Nano Energy 67 (2020) 104174

Contents lists available at ScienceDirect

Nano Energy

journal homepage: http://www.elsevier.com/locate/nanoen

Full paper

Electron density modulation of $Fe_{1-x}Co_xP$ nanosheet arrays by iron incorporation for highly efficient water splitting

Haopeng Feng [a,b], Lin Tang [a,b,*], Guangming Zeng [a,b], Jiangfang Yu [a,b], Yaocheng Deng [c], Yaoyu Zhou [c], Jingjing Wang [a,b], Chengyang Feng [a,b], Ting Luo [a,b], Binbin Shao [a,b]

[a] College of Environmental Science and Engineering, Hunan University, Changsha, 410082, China
[b] Key Laboratory of Environmental Biology and Pollution Control (Hunan University), Ministry of Education, Changsha, 410082, Hunan, China
[c] College of Resources and Environment, Hunan Agricultural University, Changsha, 410128, China

ARTICLE INFO

Keywords:
Water splitting
Active sites
Volmer-Tafel
Electronic structure
Model-structure-performance

ABSTRACT

The good performance of base metal phosphides as alternative catalysts for hydrogen evolution has attracted great attention. However, phosphorus-hydrogen bonds (P-H_{ads}) are easily formed on the surface of metal phosphides, which will severely inhibit hydrogen evolution reaction (HER). Herein, we propose a universal strategy to improve the HER activity of metal phosphides by modulating the surface electron densities. The iron modulated $Fe_{0.29}Co_{0.71}P$ nanosheet arrays exhibit an overpotential of 74 mV at 10 mA cm^{-2} and a Tafel slope of 53.56 mV dec^{-1}, which are close to the performance of noble metal catalysts in alkaline condition. The electronic interactions between cobalt and phosphorus are modulated after iron doping, resulting in more positively charged Co, which can promote adsorption and activation of H_2O molecules and will weaken P-H_{ads} bonds formed on the catalyst surfaces. Therefore, $Fe_{0.29}Co_{0.71}P$ can optimize the adsorption and desorption of H atoms, and can promote both Volmer and Heyrovsky steps of HER. In addition, the electron density modulation of catalytic sites also improves the OER catalytic performance of $Fe_{0.29}Co_{0.71}P$. The overall water splitting electrolyzer assembled by $Fe_{0.29}Co_{0.71}P$/Ni-foam exhibits a lower cell voltage (1.59 V/10 mA cm^{-2}), compared to that (1.61 V/10 mA cm^{-2}) of the IrO_2//Pt/C electrolyzer.

1. Introduction

Low-cost hydrogen production is the central tenet of building the next generation hydrogen-based energy system [1]. Water electrolysis, as one of the most effective methods for hydrogen production, still faces the problems of high cost and low efficiency of catalysts [2]. To date, noble metal catalysts, such as platinum (Pt), are still the most efficient electrocatalysts for hydrogen evolution reaction (HER), while their low crustal abundance and high cost greatly suppress their wider applications [3]. Therefore, base metal catalysts, especially transition metal compounds (metal phosphides, selenides, sulfides, and carbides, etc.), have been extensively studied as alternatives to the noble-metal Pt-based catalysts [4–7]. Inspired by the compositions and structures of the hydrogenase and nitrogenase in natural biological systems, the transition metal phosphides have attracted special attention as HER electrocatalysts [8]. For instance, Ni_2P nanoparticles were considered to be highly effective toward hydrogen evolution with an overpotential of 116 mV at 10 mA cm^{-2} in acidic condition [9]. The MoP nanoparticles with superior chemical stability and metallic properties showed an overpotential of 180 mV at 30 mA cm^{-2} for HER [10]. Although the efficiencies of the obtained metal phosphide are still far lower than those of Pt-based catalysts, the current studies reveal that transition metal phosphides with adjustable surface properties have great prospects for the development of effective HER catalysts.

CoP with outstanding electrical conductivity, versatile redox nature and hybrid d orbitals, has attracted considerable attention [11–17]. Unfortunately, the alkaline catalysis of CoP is inactive due to the sluggish water adsorption and dissociation dynamics, which is essentially determined by its inherent structural nature [18]. For metal phosphides, P-H_{ads} bonds are easily formed on the surfaces of electrocatalysts during HER, which is beneficial for H adsorption. However, the interaction between the electronegative phosphorus and adsorbed H_{ads} are usually so strong that makes the H_{ads} difficult to desorb to form H_2. Furthermore, the coordination state of metal phosphides will be saturated with the evolution of hydrogen, making it more difficult for H_2O adsorption. Despite the morphological engineering can promote the HER activity of

* Corresponding author. College of Environmental Science and Engineering, Hunan University, Changsha, 410082, China.
E-mail address: tanglin@hnu.edu.cn (L. Tang).

https://doi.org/10.1016/j.nanoen.2019.104174
Received 6 May 2019; Received in revised form 22 August 2019; Accepted 5 October 2019
Available online 19 October 2019
2211-2855/© 2019 Elsevier Ltd. All rights reserved.

metal phosphides to a certain extent through increasing the catalytic sites, it cannot essentially change the intrinsic catalytic nature of metal phosphides, and it is also hard to directly weaken the P-H_{ads} bonds. Recently, some studies found that the HER activities of the metal phosphides can be further improved by the introduction of other promoter species to form binary phosphides. For instance, incorporation of Ni into CoP to form CoNiP could efficiently improve the HER activity, achieving 80 mV at 10 mA cm^{-2} [19]. In addition, Zhang et al. [20] reported that Fe-doped NiP nanosheets as stable and highly active electrocatalysts for HER exhibit a low overpotential of 104 mV at 10 mA cm^{-2}. However, we found that the understanding of the essences of alkaline catalysis, especially at atomic levels, is absent. In addition, most of metal phosphides only showed an enhanced performance in the HER process, but their performance for both OER and HER in the same electrolyte has rarely been reported. Thus, promoting the HER catalytic activity of metal phosphides to the level of noble-metal catalysts through rationally regulating the electronic density of catalytic sites and unraveling the essences of modulation mechanism is highly desirable but challenging.

Here we propose a facile and universal strategy to modulate the electron densities of the catalytic sites of $Fe_{1-x}Co_xP$ nanosheet arrays for high performance HER activity by using iron as the modulator. The design principle is to increase the positive charge of metal sites by iron incorporation which is conducive to adsorbing water molecules and promoting H-O cleavage. The more negatively charged phosphorus can strengthen M-P (M = Co and Fe) bonds and thus will weaken P-H_{ads} bonds. Therefore, it can optimize adsorption and desorption of H. The Fe-modulated $Fe_{1-x}Co_xP$ exhibits superior catalytic activity and stability toward HER as well as OER in alkaline media. The experimental results, characterization means and density functional theory (DFT) studies consistently demonstrate that the d-band centers and surface electron densities of $Fe_{1-x}Co_xP$ can be effectively modulated by Fe doping. To further reveal the effects of Fe doping on the HER catalytic process, DFT simulation suggests that the Fe incorporation could not only promote desorption of H_{ads} from P sites but also boost the dissociation of water molecules. Moreover, we also demonstrate that the Fe modulation is a universal strategy to consistently improve the HER catalysis of various metal phosphides, metal sulfides and metal selenides. The ability to manipulate the d band centers and electron densities of the catalytic sites through rational surface engineering could offer a new insight for the development of highly efficient HER catalysts beyond.

2. Experimental section

2.1. Material synthesis

All chemicals were analytical grade and were used as received without further purification. The synthesis of $Fe_{1-x}Co_xP$/Ni-foam is composed of the following steps.

2.1.1. Synthesis of $Fe_{1-x}Co_x$-layered double hydroxide/Ni-foam ($Fe_{1-x}Co_x$-LDH/NF)

A piece of Ni-foam (NF) was degreased in acetone solution and etched in 3.0 M HCl solution with sonication for 10 min, respectively, and subsequently washed thoroughly with deionized water and ethanol to ensure a clean surface. After drying under natural conditions, the weight of each treated NFs was recorded. $Fe_{1-x}Co_x$-LDH nanosheets arrays with different Fe/Co ratios were synthesized on NFs through a hydrothermal process. In a typical synthesis, 10 mmol of urea, 8 mmol of NH_4F, and 1.4 mmol of metal salts ($Fe(NO_3)_3{\cdot}9H_2O$ and $Co(NO_3)_2{\cdot}6H_2O$) with different mole ratios of Fe/Co were dissolved in 40 mL deionized water to form a clear solution under constant stirring. Then the pre-treated NF was transferred into a Teflon-lined stainless steel autoclave (80 mL) containing the above solution and maintained at 120 °C for 12 h. After natural cooling, the $Fe_{1-x}Co_x$-LDH loaded NF was taken out, washed by deionized water and ethanol, and finally dried at 60 °C under vacuum. The mass loading of the $Fe_{1-x}Co_x$-LDH/NF catalyst can be seen in Table S1.

2.1.2. Synthesis of $Fe_{1-x}Co_xP$/NF

$Fe_{1-x}Co_xP$ were obtained by phosphorizaion using PH_3, and the experimental details are as follows: the prepared $Fe_{1-x}Co_x$-LDH/NF and 1 g NaH_2PO_2 were respectively put at two separate positions of the tube furnace in two porcelain boats with the phosphate powder at the upstream side, and then heated at 350 °C using a 2 °C min^{-1} ramp rate and held at this temperature for 60 min under N_2 atmosphere. The mass loading of the $Fe_{1-x}Co_xP$/NF catalyst can be seen in Table S1.

2.1.3. Synthesis of $Fe_{1-x}Co_xS_2$/NF

The as-obtained $Fe_{1-x}Co_x$-LDH/NF was immersed in 40 mL of aqueous solution containing 150 mg of thioacetamide, and then the mixture was transferred to a Teflon-lined stainless steel autoclave (80 mL) and maintained at 140 °C for 5 h. After natural cooling, the obtained $Fe_{1-x}Co_xS_2$/NF were taken out and washed with ethanol and deionized water several times, respectively, and then dried at 60 °C under vacuum. The mass loading of the $Fe_{1-x}Co_xS_2$ catalyst can be seen in Table S1.

2.1.4. Synthesis of $Fe_{1-x}Co_xSe_2$/NF

Se powder (0.118 g) was put into deionized water (3 mL) containing $NaBH_4$ (0.130 g), and then stirred for 30 min to generate NaHSe. The freshly produced NaHSe solution was then added into absolute ethanol (40 mL) under N_2 flow to avoid the formation of NaHSe oxides. The as-obtained solution and $Fe_{1-x}Co_x$-LDH precursor were transferred into a Teflon-lined stainless steel autoclave (80 mL) and maintained at 150 °C for 16 h. After natural cooling, the obtained $Fe_{1-x}Co_xSe_2$/NF were taken out and washed with ethanol and deionized water several times, respectively, and then dried at 60 °C under vacuum. The mass loading of the $Fe_{1-x}Co_xSe_2$ catalyst can be seen in Table S1.

2.2. Characterizations

The morphology and structural of as-prepared products were investigated with scanning electron microscope (SEM, LEO 1450VP) and energy-dispersive X-ray spectroscopy (EDX, INCA 300). Transmission electron microscopy (TEM) and HRTEM images were taken by a JEOL-2100F electron microscope operated at 200 kV. The X-ray diffractometer (XRD) was obtained on a Bruker D8 Advance X-ray diffractometer (Cu Ka radiation, $\lambda = 1.54178$ Å). X-ray photo-electron spectroscopy (XPS) was collected with a Kratos ASIS-HS X-ray photoelectron spectroscope (15 kV, 10 mA). Element content was determined by inductively coupled plasma mass spectrometry (ICP-MS, Thermo Scientific iCAP6300) analysis.

2.3. Electrochemical measurements

The electrocatalytic properties of obtained samples were performed in a three-electrode system using $Fe_{1-x}Co_xM$/NF as working electrode, a carbon rod and Ag/AgCl electrode used as the counter electrode and the reference electrode, respectively. For comparison, the commercial catalyst powders IrO_2 and Pt/C (20%) were loaded on NF with 4.0 mg/cm^2, respectively. Prior to recording the polarization curves, all samples were activated by the CV test at 20 mV s^{-1}. All voltages and potentials were *iR* corrected unless otherwise specified. The potential were corrected according to the following equation: $P_{vs.RHE} = P_{vs.Ag/AgCl} + 0.059*pH - I*R_s$, where $P_{vs.RHE}$ is the potential versus standard hydrogen electrode. $P_{vs.Ag/AgCl}$ is the measured potential with Ag/AgCl electrode as reference electrode. R_s is the electrolyte resistance and I is the current density. Polarization curves were obtained using linear sweep voltammetry (LSV) curves at a scan rate of 5 mV s^{-1}. The electrochemical impedance spectroscopy (EIS) was tested at −0.30 V and 0.40 V vs RHE from 10 kHz to 0.01 Hz with a 10 mV AC amplitude for HER and OER,

respectively. The stability test for HER was operated at 10, 20, 50, 100 mA cm^{-2} under vigorous stirring for 10 h each. The stability test for OER was conducted at 50 and 100 mA cm^{-2} under vigorous stirring for 25 h each. All the potentials measured were vs. RHE. In 1.0 M KOH, $E_{RHE} = E_{Ag/AgCl} + 0.05916*pH + 0.197$. For overall water splitting measurement, $Fe_{0.29}Co_{0.71}P$/NF was employed as cathode and anode, respectively. LSV curve was also recorded at a scan rate of 5 mV s^{-1} between 1.3 and 2.0 V. The stability test was also carried out under vigorous stirring by a stir bar for 50 h.

2.4. Calculations

All calculations in this study were performed using the VASP [21, 22]. We used the PBE functional for the projector augmented wave (PAW) potential [23,24] and exchange-correlation energy [25]. The kinetic energy cutoff was set to 400 eV. The k-points meshes were sampled based on the Gaussian method. To minimize the undesired interactions between images, a vacuum of at least 15 Å was considered along the z axis. DFT simulations performed were based on the experimentally crystal structure of CoP [25] (a = 5.077 Å, b = 3.281 Å, c = 5.587 Å, ICSD collection code # 43249). The structures of FeP, $Fe_{0.25}Co_{0.75}P$, $Fe_{0.5}Co_{0.5}P$, and $Fe_{0.75}Co_{0.25}P$ were obtained by substituting cobalt atom within the unit cell with Fe atoms in all possible geometries and selected most stable ones. Chemisorption was modeled on the CoP, FeP, $Fe_{0.25}Co_{0.75}P$, $Fe_{0.5}Co_{0.5}P$, and $Fe_{0.75}Co_{0.25}P$ (101) surfaces. The surfaces were constructed as slab consisting of three layers within periodic boundary conditions, separated by a 20 Å vacuum layer. For these calculations, three layers with 2 × 2 × 1 k-Point mesh were used in the 2 × 2 super cells for CoP, FeP, $Fe_{0.25}Co_{0.75}P$, $Fe_{0.5}Co_{0.5}P$, and $Fe_{0.75}Co_{0.25}P$. Meanwhile, the calculation method of adsorption free energy for adsorbates (ΔG_{ads}) can be seen in SI in detail.

3. Results and discussion

The schematic diagram illustrates the synthesis process of the 3D $Fe_{1-x}Co_xP$ nanosheet networks on NF substrates (Fig. 1). NF was used as the substrate and current collector, and as proved by SEM image in Fig. S1, the NF is consisted of 3D conductive network and macropores. Firstly, a series of $Fe_{1-x}Co_x$-LDH nanosheet arrays with different Fe/Co mole ratio (e.g., 1/0, 0.86/0.14, 0.71/0.29, 0.57/0.43, 0.29/0.71, and 0/1) were deposited on NF by adjusting the dosage of iron and cobalt precursors under a hydrothermal condition in an aqueous solution. After hydrothermal treatment, the color of NF turned from silver to yellow-green at high Fe/Co feed ratio or rose-red at low Fe/Co feed ratio (Fig. S2a). The SEM and XRD images of $Fe_{1-x}Co_x$-LDH nanosheet arrays on NF grown with a Fe/Co ration of 0.29/0.71 (denoted as $Fe_{0.29}Co_{0.71}$-LDH/NF) are shown in Fig. S3. The interconnected and vertically-grown arrays on the NF framework are conducive to make full contact with electrolyte and accelerate the electrons transfer, which is undoubtedly beneficial to electrocatalysis. Then, $Fe_{1-x}Co_xP$/NFs were prepared by heat-treatment of $Fe_{1-x}Co_x$-LDH/NF in PH_3 atmosphere at 350 °C for 1 h. After reaction, the color of $Fe_{1-x}Co_x$-LDH/NF turned to black (Fig. 1 and Fig. S2b). SEM images of $Fe_{1-x}Co_xP$/NF with a Fe/Co ratio of 0.29/0.71 (denoted as $Fe_{0.29}Co_{0.71}P$/NF) are shown in Fig. 2a and Fig. S4 which present the uniform coating of $Fe_{0.29}Co_{0.71}P$ nanosheet arrays with a rough surface on NF. The phosphorization treatment resulted in deformation and roughness of the nanosheets, and its thickness was significantly reduced from 80–100 nm to about 30 nm (Fig. S5). Different from the "flower-liked" CoP/NF, $Fe_{0.29}Co_{0.71}P$/NF has nanosheet array structure similar to FeP/NF, $Fe_{0.29}Co_{0.71}$-LDH/NF and $Fe_{0.71}Co_{0.29}P$/NF (Figs. S3–S8). The atomic ratios of Fe and Co in the as-prepared samples were determined by energy-dispersive X-ray spectroscopy analysis (Fig. 2b), where the obtained Fe:Co ratio is approximate to the ratio of original materials (Table S2). To further verify the difference of diffraction patterns between the matric phases and $Fe_{0.29}Co_{0.71}P$, the XRD patterns of the bare CoP, FeP, and $Fe_{0.29}Co_{0.71}P$ were measured to study their crystal structures (Fig. S9). The result exhibits that the diffraction peaks of the (020), (101), (111), (200), (221), (131), and (220) lattice planes of the $Fe_{0.29}Co_{0.71}P$ sample coincided well with the calculated XRD results. When 21% Co atoms in the CoP lattice were substituted by Fe atoms, the diffraction peaks of the $Fe_{0.29}Co_{0.71}P$ showed a slight shift toward higher angles, which was ascribed to the altered fringe lattice distance of CoP

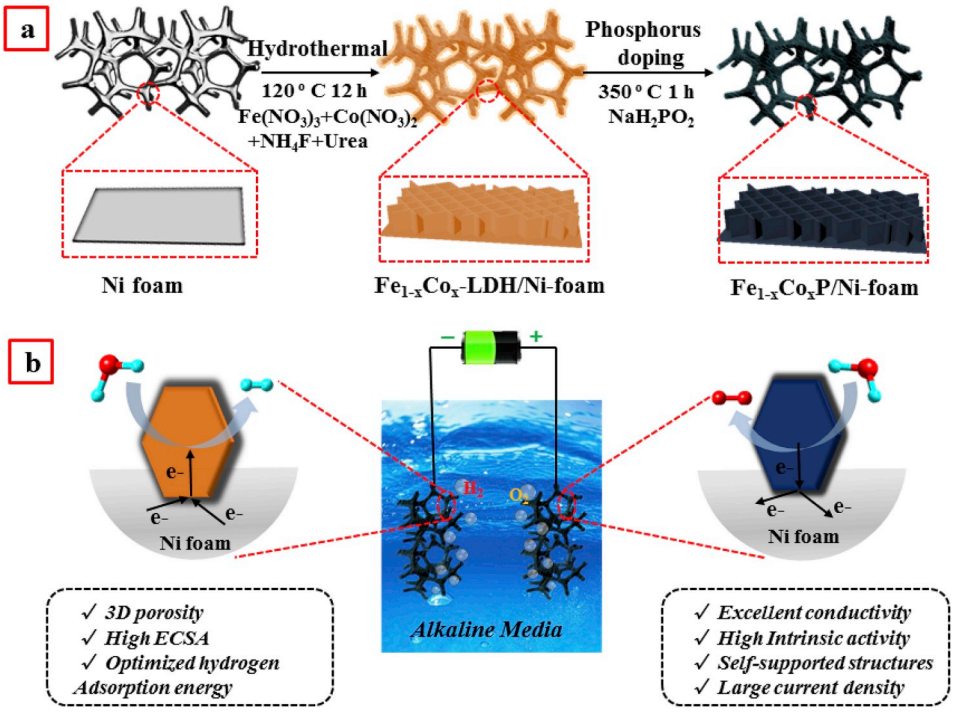

Fig. 1. (a) Schematic illustration of the two-step method for synthesizing 3D-networked $Fe_{1-x}Co_x$-LDH/NF and $Fe_{1-x}Co_xP$/NF electrodes, (b) Optical images of initial NF, as-prepared $Fe_{1-x}Co_x$-LDH/NF and $Fe_{1-x}Co_xP$/NF, respectively.

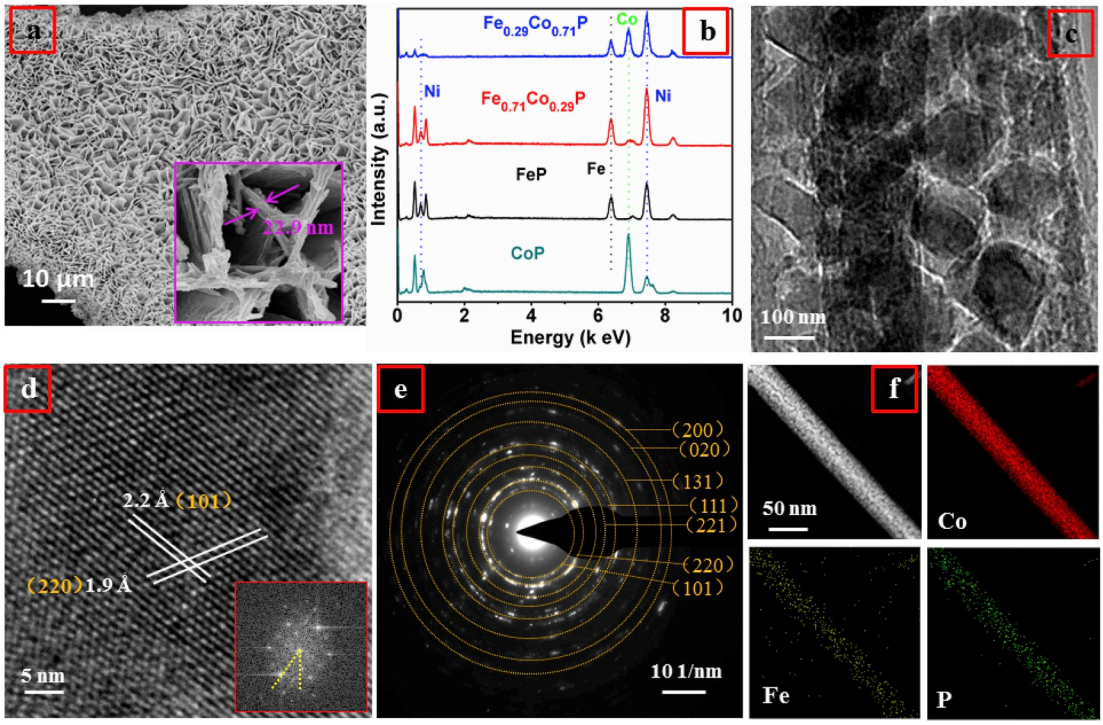

Fig. 2. (a) SEM images of $Fe_{0.29}Co_{0.71}P$/NF, (b) EDX spectrum of FeP, CoP, $Fe_{0.29}Co_{0.79}P$, and $Fe_{0.71}Co_{0.21}P$, (c) TEM images of one single $Fe_{0.29}Co_{0.79}P$ nanosheet, (d) HRTEM image and (e) SAED pattern taken from $Fe_{0.29}Co_{0.79}P$ nanosheet, (f) STEM image and EDX element mapping of Fe, Co, and P for $Fe_{0.29}Co_{0.79}P$ nanosheet.

crystalline lattice by the incorporated Fe atoms owing to the disparity in the atomic radii of Fe and Co. The TEM image of $Fe_{0.29}Co_{0.71}P$ (Fig. 2c) shows a sheet-like morphology coated with amorphous-like shells (≈3 nm) (Fig. S10). It might be attributed to the generation of phosphates owing to the oxidation by air under a long-time exposure. This unique shell structure might protect the inner $Fe_{0.29}Co_{0.71}P$ from being etched to some degree, and could also promote the electrocatalytic activity by accelerating the electron transfer from the metallic inner $Fe_{0.29}Co_{0.71}P$ to the outer shell [26–28]. The clear lattice fringes with spacing of 0.19 and 0.22 nm can be readily ascribed to the (101) and (220) crystal planes of the $Fe_{0.29}Co_{0.71}P$ phase, respectively, which proves the formation of crystalline $Fe_{0.29}Co_{0.71}P$ (Fig. 2d). The selected area electron diffraction (SAED) pattern of $Fe_{0.29}Co_{0.71}P$ nanosheet in Fig. 2e presents a series of diffraction rings indexed to the crystal planes of $Fe_{0.29}Co_{0.71}P$, which is consistent with the XRD results and revealed the polycrystalline nature of $Fe_{0.29}Co_{0.71}P$ nanosheet. The elemental mapping under both low and high magnifications (Fig. S11 and Fig. 2f) show the homogeneous distribution of Fe, Co, O and P elements on the

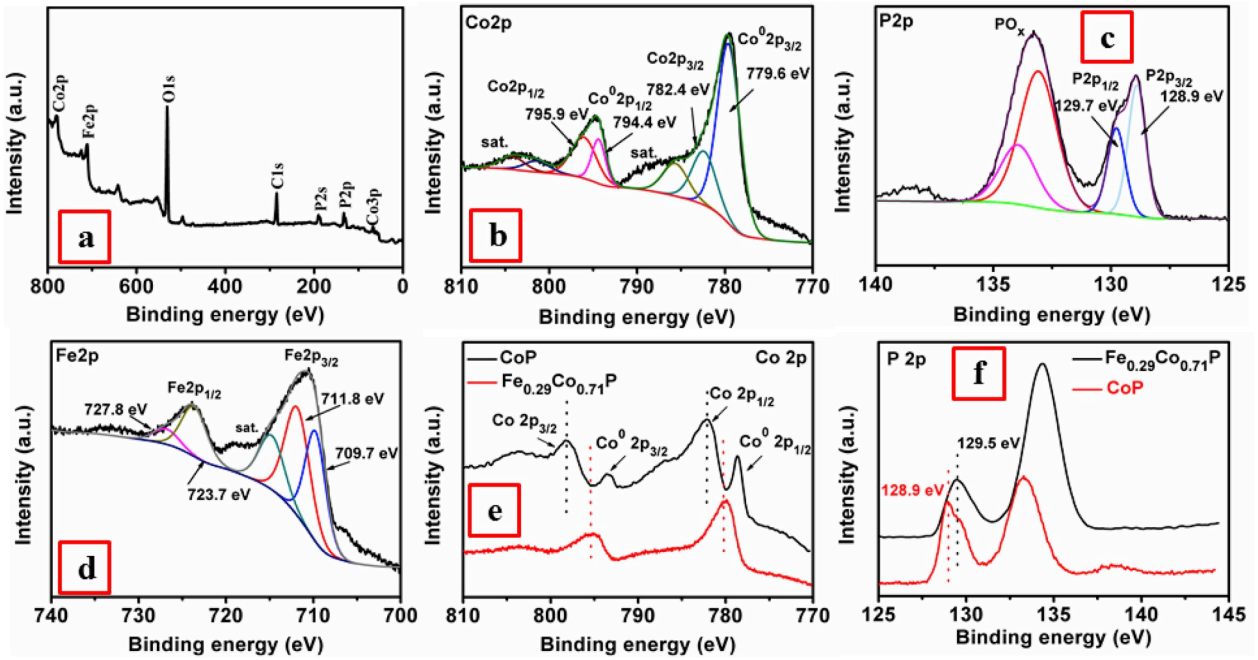

Fig. 3. (a) XPS survey spectrum for $Fe_{0.29}Co_{0.71}P$. (b) Co 2p, (c) P2p, and (d) Fe2p. XPS spectra of $Fe_{0.29}Co_{0.71}P$ and CoP: (e) Co2p, (f) P2p.

whole nanosheet (the picture shows the side of the nanosheet because the shooting angle is not well chosen in Fig. 2f). It might be beneficial for the uniform distribution of active sites on $Fe_{0.29}Co_{0.71}P$ surface and further demonstrates the distribution of phosphates.

The XPS was carried out to determine oxidation state and surface composition of $Fe_{0.29}Co_{0.71}P$, which further confirms the existence of Fe, Co, and P elements in $Fe_{0.29}Co_{0.71}P$ compounds (Fig. 3a). The Co 2p spectra exhibit two spin orbital doublets at 782.4 and 795.9 eV attributed as the binding energies for Co in the $Fe_{0.29}Co_{0.71}P$. The peaks at 779.6 and 794.4 eV are recognized as Co $2p_{3/2}$ and Co $2p_{1/2}$, respectively, which are attributed to Co^0 [29,30], with three shakeup satellites (defined as "Sat") (Fig. 3b). It displays two peaks at 128.9 and 129.7 eV corresponding to the binding energies of P $2p_{3/2}$ and P $2p_{1/2}$, respectively, which could be assigned to the phosphide (Fig. 3c) [29]. Furthermore, two spin-orbit doublets of Fe 2p are shown in Fig. 3d, where the peaks at 709.7 and 723.7 eV correspond to the Fe^{2+} arising from the Fe-P bonding structures, and peaks at 711.8 and 727.8 eV correspond to the Fe^{3+} deriving from the iron phosphate (Fe-PO_x). The fact that the characteristic peak of FeP is not observed in Fe 2p spectra [31] indicates the existence of a ternary $Fe_{0.29}Co_{0.71}P$ compound instead of a mixture of two spin orbital phases. According to the fitted XPS of $Fe_{0.29}Co_{0.71}P$, the binding energy for Co 2p (795.1 eV) is lower than the Co (796.6 eV) in CoP, and the binding energy for P 2p (129.5 eV) is higher than the corresponding elemental P (128.9 eV) in CoP (Fig. 3e and f). The binding energy of Co in $Fe_{0.29}Co_{0.71}P$ is negatively shifted and the binding energy of P is positively shifted, indicating strong electron interactions between Co and Fe, which may have great significance in improving the catalytic reaction [32].

The HER electrocatalytic activity of $Fe_{0.29}Co_{0.71}P$/NF nanosheet arrays is studied in alkaline solution (1 M KOH, pH 14), and the results are shown in Fig. 4a (The mass loading of $Fe_{1-x}Co_xP$ nanosheet arrays on the NF are shown in Table S2). Commercial Pt/C (20%) catalyst with a mass of 4.0 mg/cm^2 on the NF is also investigated as the benchmark catalyst. As shown in Fig. 4a, the Pt/C on NF exhibits excellent performance, while bare NF has poor HER activity within the window of potential examined. Remarkably, $Fe_{0.29}Co_{0.71}P$/NF electrode shows Pt-like HER activity with the overpotential (74 mV) close to that of commercial Pt/C (21 mV) at the geometric current density of 10 mA cm^{-2} (η_{10}), which is much lower than that of bare FeP (193 mV), CoP (155 mV), $Fe_{0.29}Co_{0.71}$-LDH (199 mV), and NF (218 mV) at the same condition. Compared to the FeP/NF, CoP/NF owned better HER activity, but $Fe_{0.29}Co_{0.71}P$/NF exhibits the highest HER activity, demonstrating that Fe doping can effectively improve the catalytic activity of CoP. Furthermore, the stoichiometry of $Fe_{1-x}Co_xP$ has important influence on the catalytic performance. The polarization curves of $Fe_{1-x}Co_xP$ nanosheet arrays with different mole ratios of Fe/Co are shown in Fig. S12a, where the $Fe_{0.29}Co_{0.71}P$ nanosheet arrays exhibited the lowest overpotential compared to its counterparts at the geometric current density of 10 mA cm^{-2}, such as $Fe_{0.86}Co_{0.14}P$/NF (112 mV), $Fe_{0.71}Co_{0.29}P$/NF (108 mV), $Fe_{0.57}Co_{0.43}P$/NF (98 mV), and $Fe_{0.10}Co_{0.90}P$/NF (90 mV). The HER activity of $Fe_{1-x}Co_xP$ nanosheet arrays increased first and then decreased when the content of Fe was up to 29%, which further demonstrates that the doping with proper content of iron into CoP/NF can improve the HER activity. In addition, to further explore the reason why $Fe_{0.29}Co_{0.71}P$/NF is superior to Pt/C/NF at high current density, the adhesion effect of gas bubbles on different electrodes used for the HER was observed and the surface wettability of the electrodes was also tested (Fig. S13). These results revealed the super-hydrophilic nature of $Fe_{0.29}Co_{0.71}P$/NF electrode and demonstrated that the $Fe_{0.29}Co_{0.71}P$/NF electrode can accelerate the desorption behavior of hydrogen gas bubbles in the HER process. (See SI for more details) Specifically, the overpotentials at the geometric current densities of 10, 50, and 200 mA cm^{-2} for $Fe_{0.29}Co_{0.71}P$/NF were 74, 112, and 116 mV, respectively, which is superior to many Co phosphides and Fe phosphides catalysts, including CoP/CNT ($\eta_{10}^{-2\ \text{mA}\ \text{cm}} = 122$ mV) [12], Co_2P branched nanostructures ($\eta_{10}^{-2\ \text{mA}\ \text{cm}} = 120$ mV) [33], CoP/rGO-400 ($\eta_{10}^{-2\ \text{mA cm}} = 105$ mV) [34], Co_2P/Ti ($\eta_{10}^{-2\ \text{mA cm}} = 95$ mV) [35], Fe-O-P NRs ($\eta_{10}^{-2\ \text{mA}\ \text{cm}} = 96$ mV) [36], FeP/Ti foil ($\eta_{10\ \text{mA}}$

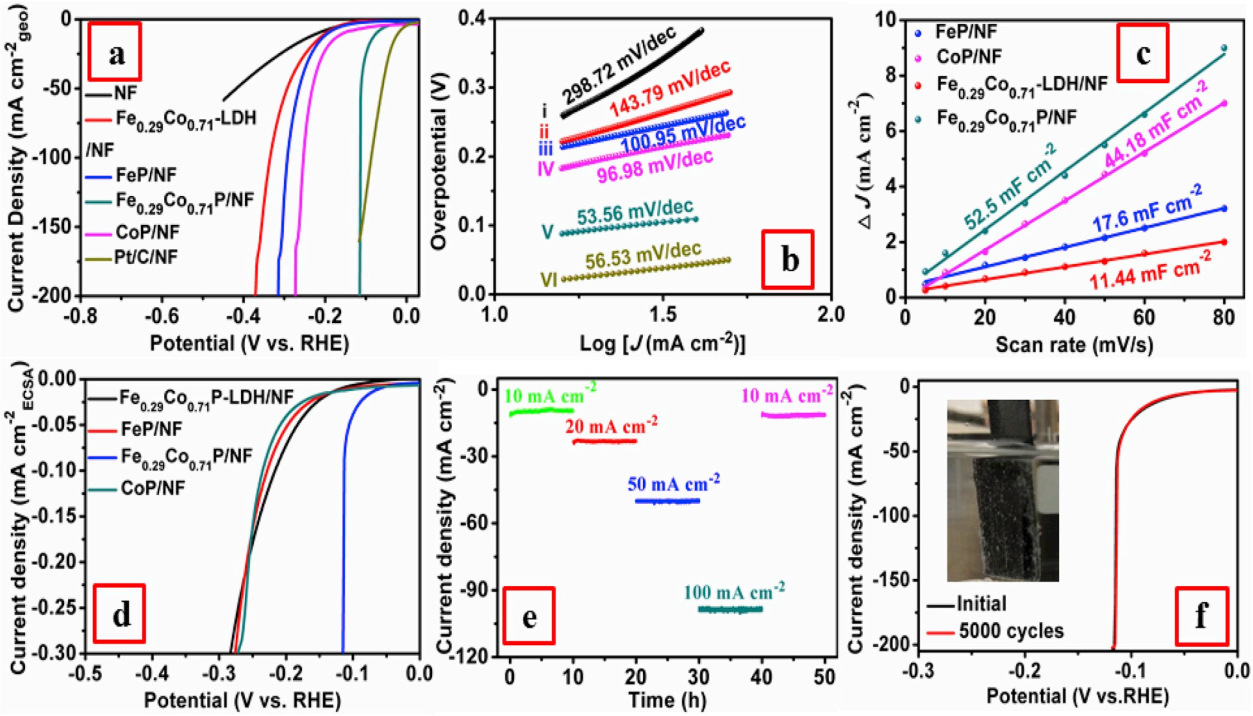

Fig. 4. (a) LSV curves for bare NF, Pt/C on NF, and $Fe_{1-x}Co_xP$/NF with a scan rate of 5 mV s^{-1} for HER, (b) Tafel plots for bare NF, Pt/C on NF, and $Fe_{1-x}Co_xP$/NF, (c) capacitive currents as a function of scan rate for $Fe_{1-x}Co_xP$/NF, (d) LSV from (a) normalized to the ECSA, (e) chronoamperometry curve of $Fe_{0.29}Co_{0.79}P$/NF recorded at different current densities for a total duration of 50 h, (f) LSV curves for $Fe_{0.29}Co_{0.79}P$/NF before and after 5000 CV cycles, and the inset exhibits the photo taken during HER catalytic process at an overpotential of 112 mV.

$_{cm}{}^{-2}$ = 102 mV) [37], FeP NP/CC (η_{10}^{-2} $_{mA\ cm}$ = 115 mV) [38], and FeP NAs (η_{10}^{-2} $_{mA\ cm}$ = 202 mV) [39]. It is noteworthy that the $Fe_{0.29}Co_{0.71}P$/NF also exhibits great superiority to other recently reported base-metal HER electrocatalysts (Table S3).

The Tafel plots of $Fe_{0.29}Co_{0.71}P$/NF is 53.56 mV dec^{-1}, lower than that of bare NF (298.72 mV dec^{-1}), Pt/C/NF (56.53 mV dec^{-1}), CoP/NF (96.98 mV dec^{-1}), FeP/NF (100.95 mV dec^{-1}), and $Fe_{0.29}Co_{0.71}$-LDH/NF (143.79 mV dec^{-1}), which indicates the Volmer-Heyrovsky reaction mechanism in the $Fe_{0.29}Co_{0.71}P$/NF sample (Fig. 4b). Meanwhile, compared to the $Fe_{0.86}Co_{0.14}P$/NF (100 mV dec^{-1}), $Fe_{0.71}Co_{0.29}P$/NF (87.64 mV dec^{-1}), $Fe_{57}Co_{0.43}P$/NF (68.31 mV dec^{-1}), $Fe_{57}Co_{0.43}P$/NF (89.04 mV dec^{-1}) and CoP/NF, the lower Tafel slope of $Fe_{0.29}Co_{0.71}P$/NF further proves that the doping with proper content of iron can effectively improve the HER activity (Fig. S12b) (the comparison data with other electrocatalysts are introduced in Table S3 with H_2 production beyond 100 mA cm^{-2}). Generally, the lower Tafel slope of $Fe_{0.29}Co_{0.71}P$/NF electrode demonstrates a better kinetics, even when considerable H_2 production is required at higher voltage or current densities. Furthermore, the decrease of Tafel slope from 96.98 mV dec^{-1} (CoP/NF) to 53.56 mV dec^{-1} ($Fe_{0.29}Co_{0.71}P$/NF) might be attributed to a possible modification effect of the surface electronic state by the doped Fe elements, which can improve the intrinsic electrical conductivity of the catalysts and weaken P-H_{ads} to generate more H_2 [40].

However, while the geometric area current density is often used to evaluate the total electrode activity, it may not be the most suitable measure of the intrinsic activity due to the lack of consideration of the electrochemically active surface area (ECSA). Thus, the ECSAs of FeP/NF, CoP/NF, $Fe_{0.29}Co_{0.71}P$-LDH/NF, and $Fe_{0.29}Co_{0.71}P$/NF were determined by the double layger capacitance (C_{dl}) (Fig. S14). In Fig. 4c, the C_{dl} of $Fe_{0.29}Co_{0.71}P$/NF is larger than those of FeP/NF, CoP/NF, and $Fe_{0.29}Co_{0.71}P$-LDH/NF, suggesting the more electrochemical active sites for $Fe_{0.29}Co_{0.71}P$/NF. LSVs presented in Fig. 4d were normalized to the ECSA and calculated from C_{dl} (See SI for details) by Fig. 4c, where $Fe_{0.29}Co_{0.71}P$/NF still shows the best catalytic activity. It proves that the $Fe_{0.29}Co_{0.71}P$ has the highest intrinsic activity compared to its counterparts. The exchange current density of $Fe_{0.29}Co_{0.71}P$/NF is 0.389 mA cm^{-2} calculated by extrapolating the Tafel plot to $\eta = 0$ V, which is 2.6 times of that of CoP/NF (0.151 mA cm^{-2}) (Fig. S15) and outperforms many reported catalysts (Table S3). Electrochemical impedance spectroscopy (EIS) measurements of $Fe_{0.29}Co_{0.71}P$/NF were performed at different potentials from 0.01 Hz to 10 kHz with amplitude of 10 mV in 1.0 M KOH (Fig. S16a). The semicircles in the low- and the high-frequency range of the Nyquist plot are attributed to the solution resistance and charge transfer resistance (R_{ct}), respectively. The R_{ct} of $Fe_{0.29}Co_{0.71}P$/NF is much lower than those of CoP/NF, FeP/NF, and $Fe_{0.29}Co_{0.71}$-LDH/NF under the overpotential of 250 mV, which implied that rapid electron transfer happens as shown in Fig. S16b. Thus, the improved HER activity of $Fe_{0.29}Co_{0.71}P$/NF compared to its counterparts can be ascribed to large ECSAs and small electronic/mass transfer resistances. All these improvements can be attributed to the electronic structure modification of $Fe_{0.29}Co_{0.71}P$ by Fe doping. In addition, we tried to quantify the active sites by rough calculation of turnover frequency (TOF) to compare the intrinsic activities of $Fe_{0.29}Co_{0.71}P$ with those of other electrocatalysts. It is difficult to determine the quantity and nature of catalytically active sites on the rough electrodes surface, so relatively accurate TOF by reasonable calculation was required to obtain. Here, we calculated the TOF on CoP/NF, FeP/NF, and $Fe_{0.29}Co_{0.71}P$/NF at an overpotential of 74 mV through assuming 100% participation of all the Co atoms in the CoP/NF and $Fe_{0.29}Co_{0.71}P$/NF, and Fe atoms in the FeP/NF. Detailed calculations of the quantity of Co and Fe atoms and the TOF values can be found in the Supporting Information. The calculated TOF values for $Fe_{0.29}Co_{0.71}P$, CoP and FeP are 1.08 s^{-1}, 0.416 s^{-1} and 0.142 s^{-1}, respectively (Fig. S17), where the higher TOF calculated for $Fe_{0.29}Co_{0.71}P$ at the same potential highlights its excellent electrocatalytic HER activity over CoP/NF and FeP/NF. To further evaluate the activity of $Fe_{0.29}Co_{0.71}P$ alone for the HER catalysis, we deposited $Fe_{0.29}Co_{0.71}P$ on a carbon cloth with a similar mass loading, and the $Fe_{0.29}Co_{0.71}P$/CC still exhibited outstanding performance under similar test conditions. We also carried out additional comparative experiments to confirm the role of $Fe_{0.29}Co_{0.71}P$ in HER catalysis. The $Fe_{0.29}Co_{0.71}P$ layer in the $Fe_{0.29}Co_{0.71}P$/NF electrode was removed through immersing the electrode in an HCl solution (1 M). The HER acitivity of $Fe_{0.29}Co_{0.71}P$ evidently decreased after $Fe_{0.29}Co_{0.71}P$ removal (Fig. S18). This further confirms that $Fe_{0.29}Co_{0.71}P$ itself is an active material for HER.

To explore the electrochemical durability of electrocatalysts, the chronoamperometry measurements of HER on $Fe_{0.29}Co_{0.71}P$/NF electrode were carried out under different overpotentials. Noticeably, the current density remained almost unchanged for each overpotential during 50 h tests, suggesting a superior electrochemical stability of $Fe_{0.29}Co_{0.71}P$/NF electrode in alkaline condition (Fig. 4e). The photograph exhibited a large amount of small bubbles escaping from the electrode surface with the overpotential of 114 mV, suggesting the generation of massive hydrogen which was easily detached from the electrode surface (inset in Fig. 4f). After 5000 voltammetry cycles, the polarization curve of $Fe_{0.29}Co_{0.71}P$/NF exhibited almost the same as the original (Fig. 4f). In addition, SEM images and XPS spectra of $Fe_{0.29}Co_{0.71}P$ are shown in Fig. S19 and Fig. S20, respectively, exhibiting that the surface morphology, structure, and chemical state of $Fe_{0.29}Co_{0.71}P$ are hardly changed after the constant HER for 50 h. Therefore, in contrast to pure CoP and FeP, the $Fe_{0.29}Co_{0.71}P$ with higher HER stability and more rapid HER kinetics further proved a remarkable effect of Fe doping in $Fe_{1-x}Co_xP$ for HER activity improvement. To further demonstrate that the Fe doping is a general strategy to improve the HER catalysis, $Fe_{1-x}Co_xSe_2$/NF electrode and $Fe_{1-x}Co_xS_2$/NF electrode were successfully synthesized. As shown in Fig. S21, the shape of the nanosheets was changed to nanowire arrays in $Fe_{1-x}Co_xSe_2$ with a homogeneous distribution of Fe, Co, and Se elements (Fig. S22). Similarly, $Fe_{0.29}Co_{0.71}S_2$ existed in a "rice-like" morphology also possessing a homogeneous distribution of Fe, Co, and S elements (Figs. S23 and S24). The experimental results further demonstrate that proper doping of Fe could improve the HER activity of $Fe_{1-x}Co_xM$ (P, Se, S) (Figs. S25 and S26).

To reveal the effects of Fe doping on the electron densities and catalytic properties of $Fe_{0.29}Co_{0.71}P$ at the atomic level, we conducted DFT calculations. Fig. 5a exhibits the top-view structure of $Fe_{0.25}Co_{0.75}P$ (101) (the Fe/Co ratio in the calculation model is similar to that in the experimental material $Fe_{0.29}Co_{0.71}P$) with the bond lengths, and the Co-P bond lengths (2.150 and 2.228 Å) are slightly decreased after iron doping compared to pure CoP (2.182 and 2.348 Å) (Fig. S27). The results demonstrate that Fe doping can effectively modulate the strength of P-Co bonds in $Fe_{0.29}Co_{0.71}P$, which is well-connected with the adsorption/desorption properties and surface electron densities of atoms. In addition, both pure CoP and $Fe_{0.29}Co_{0.71}P$ show metallic behaviors without a band gap (Fig. S28), which is consistent with results of total and summed density of states (TDOS) and partial density of states (PDOS), where the conclusion is based on the states originated from the Co atoms crossing the Fermi level. After Fe doping, Fe 3d orbitals are bonded to Co 3d orbitals and P p orbitals near Fermi level, indicating an obvious electron transfer between Co and Fe atoms (Fig. S26b). Moreover, according to the TDOS in CoP and $Fe_{1-x}Co_xP$, the peaks of $Fe_{1-x}Co_xP$ obviously become tightened (Fig. S29b, S30b and S31b). The peak of Co 3d orbitals in the $Fe_{1-x}Co_xP$ move toward lower energy near the Fermi level compared to the CoP in the PDOS. The center of Co 3d orbitals peak moves from −1.5 eV (CoP) to −1.0 eV ($Fe_{0.25}Co_{0.75}P$), −0.9 eV ($Fe_{0.5}Co_{0.5}P$), and −0.75 eV ($Fe_{0.75}Co_{0.25}P$), which is consistent with the results of Co peak negatively shifted in XPS. Furthermore, more electrons flow from metal atoms to P atoms to form strong M-P bonds, resulting in P-H_{ads} with weakened bond energy, and thus facilitating the H desorption from P sites. Proverbially, the Fermi level can reveal the ability of electron transfer or evolution on the electrocatalyst surface, and the larger the Fermi level, the higher the electron transfer capability

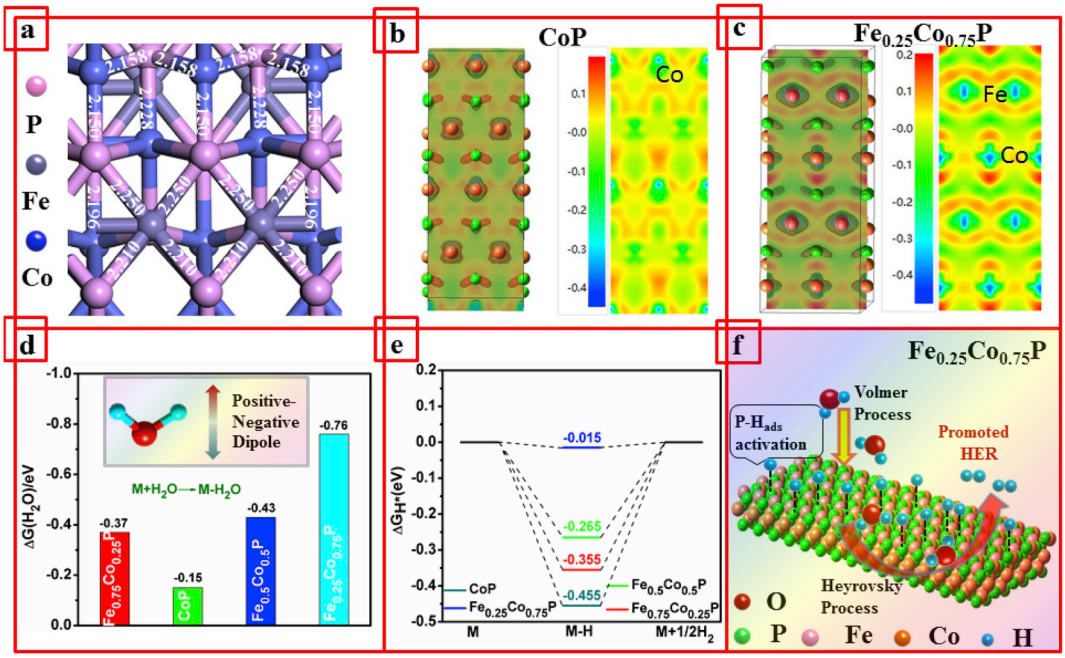

Fig. 5. DFT calculations of $Fe_{0.25}Co_{0.75}P$. (a) The top-view structures of $Fe_{0.25}Co_{0.75}P$ (101) with labeled bond lengths (Å) of Co-P and Fe-P bonds. The top-view electron density difference of (b) CoP (101), and (c) $Fe_{0.25}Co_{0.75}P$ (101), ranging from −0.4 to 0.1. The calculated adsorption free energy of H_2O (d) and H (e) on CoP (101), $Fe_{0.25}Co_{0.75}P$ (101), $Fe_{0.5}Co_{0.5}P$ (101), and $Fe_{0.75}Co_{0.25}P$ (101). (f) Schematic illustration of water adsorption, water activation, and hydrogen generation processes.

[41,42]. Compared to CoP with the Fermi level in 1.627 eV, the much larger Fermi level of $Fe_{0.25}Co_{0.75}P$ (2.087 eV) suggests that Fe doping can significantly improve the electron transfer ability of CoP. So far, the band centers, band shapes, bandwidth and overlapping are often used to evaluate the multiple properties of electrocatalysts, including the catalytic activities, stabilities, and etc. These multiple properties can also determine the performance of catalysts [43,44]. The overlap of electronic clouds of Co in $Fe_{0.25}Co_{0.75}P$ has distinctly increased compared to that of Co in the same position in pure CoP (Fig. 5b and c), where the more overlap of electronic clouds means a higher degree of electronic communization with a stronger metallicity. From Figs. S32a–S32d, electron clouds gathered in the direction of doped atoms, indicating an enhanced bonding ability of P-M bond by Fe doping. This further proved that the electronic structure of $Fe_{0.29}Co_{0.71}P$ with Fe doping is successfully modified. Moreover, compared to CoP, the positive charge of Co in $Fe_{1-x}Co_xP$ significantly increased at first, and then decreased with the increase of iron content. The trend was consistent with the exhibited HER activity of $Fe_{1-x}Co_xP$ by previous experiments. Compared to its counterparts, the electrons in $Fe_{0.25}Co_{0.75}P$ are easier to transfer from Co atoms to nearby atoms compared to its counterparts, then leading to a faster or easier adsorption of H_2O molecule by the Co-O interaction with an exothermic process. Although the positive charge of Fe in $Fe_{1-x}Co_xP$ increases with the increasing of iron content, oxygen prefers to the cobalt site. Meanwhile, considering that the H_2O is a typical polar molecule including an O atom with negative charge and two H atoms with positive charge (as inserted in Fig. 5d), the positively charged Co in $Fe_{0.29}Co_{0.71}P$ will adsorb and activate H_2O molecules through capturing oxygen atoms. Therefore, water adsorption free energies of CoP, $Fe_{0.25}Co_{0.75}P$, $Fe_{0.5}Co_{0.5}P$, and $Fe_{0.75}Co_{0.25}P$ were investigated by DFT calculations as shown in Fig. 5d, which exhibits that $Fe_{0.25}Co_{0.75}P$ has the lowest H_2O adsorption energy, indicating that the H_2O adsorption on $Fe_{0.25}Co_{0.75}P$ is easier than its counterparts. The above results suggest that $Fe_{0.25}Co_{0.75}P$ can efficiently improve water adsorption and activation, and thus will accelerate the Volmer step of HER to optimize hydrogen atoms adsorption. The modification of electronic structure of $Fe_{0.25}Co_{0.75}P$ induced by iron doping can weaken P-H_{ads} bonds generated on the electrocatalyst surfaces and will optimize H desorption to accelerate Heyrovsky step of HER. As shown in Fig. 5e, the DFT calculation results suggest that the adsorption of H on CoP is found to be too strong, resulting in low HER electrocatalytic activities on CoP. For $Fe_{0.25}Co_{0.75}P$, it has appropriate H adsorption energy, leading to high HER electrocatalytic activity. Thus, the experimental and theoretical results prove that $Fe_{0.25}Co_{0.75}P$ after Fe doping can weaken P-H_{ads} bonds and optimize H desorption. The schematic diagram in Fig. 5f explain the promotion effect of Fe doping in improving the adsorption and activation of water molecule and optimizing the adsorption and desorption of H atoms for efficient HER.

The OER activities of $Fe_{0.29}Co_{0.71}P$ were also investigated. The results confirmed that Fe doping in $Fe_{0.29}Co_{0.71}P$ could not only improve the HER activity but also enhance the OER activity. The overpotential significantly reduced from 288 mV (CoP) to 251 mV ($Fe_{0.29}Co_{0.71}P$) at the geometric current density of 50 mA cm^{-2} (Fig. 6a). The polarization curves of $Fe_{1-x}Co_xP$ nanosheet arrays with different mole ratios of Fe/Co are shown in Fig. S33, where the $Fe_{0.29}Co_{0.71}P$ nanosheet arrays also exhibited the lowest overpotential compared to its counterparts at the geometric current density of 50 mA cm^{-2}, such as $Fe_{0.57}Co_{0.43}P$ (272 mV), and $Fe_{0.71}Co_{0.29}P$ (281 mV). It suggests that the $Fe_{0.29}Co_{0.71}P$ has high catalytic efficiency of OER. Moreover, in order to evaluate the reaction kinetics of $Fe_{0.29}Co_{0.71}P$, the Tafel slopes of these electrodes are further compared (Fig. 6b). Clearly, linear fitting of Tafel plots exhibits a Tafel slope of about 37.76 mV dec^{-1} for $Fe_{0.29}Co_{0.71}P$/NF electrode, which is significantly smaller than that of pure CoP/NF (62.38 mV dec^{-1}), FeP/NF (50.5 mV dec^{-1}), IrO_2/NF (108.71 mV dec^{-1}), and pure NF (118.3 mV dec^{-1}). These results suggest that $Fe_{0.29}Co_{0.71}P$/NF electrode has rapid reaction kinetics and excellent OER performance after iron doping. The ECSAs of FeP/NF, $Fe_{0.29}Co_{0.71}P$/NF, and $Fe_{0.53}Co_{0.47}P$/NF electrode were determined by the double laryer capacitance (C_{dl}) (Fig. S34e). The C_{dl} of $Fe_{0.29}Co_{0.71}P$/NF is larger than those of FeP/NF, CoP/NF, and $Fe_{0.53}Co_{0.47}P$/NF, suggesting the more electrochemical active sites for $Fe_{0.29}Co_{0.71}P$/NF. LSVs presented in Fig. S35 is normalized to the ECSA and calculated from C_{dl} by Fig. S34e, where $Fe_{0.29}Co_{0.71}P$/NF electrode shows the best catalytic activity. It proves

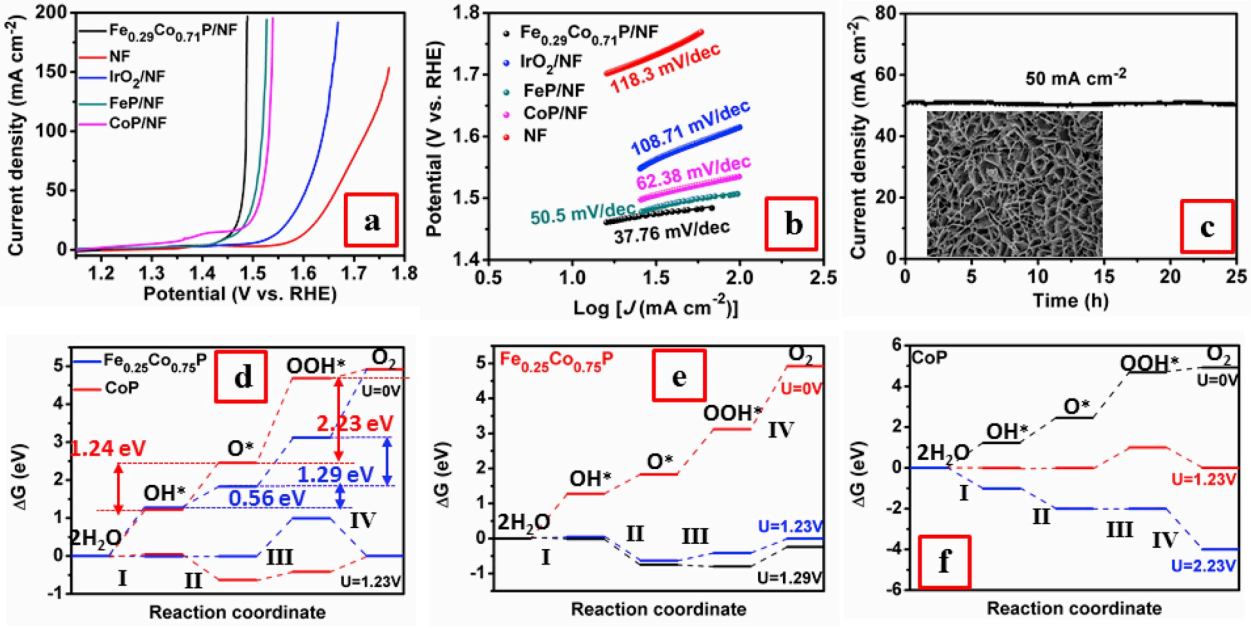

Fig. 6. (a) Polarization curves of the bare NF, FeP/NF, CoP/NF, $Fe_{0.29}Co_{0.79}P$/NF, and the commercial IrO_2/C catalyst, (b) the corresponding Tafel plots of these catalysts, (c) chronopotentiometry curves of $Fe_{0.29}Co_{0.79}P$/NF with a current density of 50 for a total duration of 25 h, (d) Gibbs free energy diagram of OER at U = 0 V and U = 1.23 V for $Fe_{0.25}Co_{0.75}P$ (Co site as the active site), CoP, (e) Gibbs free energy diagram for elementary reactions of OER over $Fe_{0.25}Co_{0.75}P$, and (f) CoP.

that the $Fe_{0.29}Co_{0.71}P$/NF has the highest intrinsic activity compared to its counterparts. Meanwhile, the Rct of $Fe_{0.29}Co_{0.71}P$/NF is much lower than those of CoP/NF, FeP/NF, and $Fe_{0.53}Co_{0.47}P$/NF under the overpotential of 200 mV, which implied that rapid electron transfer happens as shown in Fig. S34f. These results further demonstrate that the Fe doping in $Fe_{0.29}Co_{0.71}P$ can enhance the OER activity. The OER performance of $Fe_{0.29}Co_{0.71}P$ is also superior to many other high-performance OER catalysts (Table S4). The long-term durability was continuous operated at 50 mA cm^{-2} (Fig. 6c) and the anodic current density loss could be negligible even after 25 h. The XPS characterization of $Fe_{0.29}Co_{0.71}P$ after the long-term OER process was also carried out (Fig. S36). A significant change in the P 2p XPS spectra for $Fe_{0.29}Co_{0.71}P$ is observed after the long-term OER process. Specifically, a small fraction of phosphide is converted into phosphorus oxides. But the main component of the catalyst is still the phosphide of iron and cobalt, which indicates that the phosphide of iron and cobalt still plays a major role. To further reveal the intrinsic mechanism, we used DFT + U computations to analyze the overpotential and Gibbs free energy of reaction coordinate steps for OER based on the $4e^-$ mechanism of water oxidation proposed by Norskov [45] (see the Supporting Information for details). The Co site played a crucial role in $Fe_{0.25}Co_{0.75}P$ for OER catalysis, and there are many Co site with unsaturated coordination in the edge of layered bimetallic phosphide nanosheets, thus the Co site in the (101) crystal plane was considered as the main active site of $Fe_{0.25}Co_{0.75}P$ for DFT + U computations. The free energy diagrams of the reaction intermediates in the Gibbs free energy are exhibited in Fig. 6d and Fig. S37. The intermediates, *OH, *O, and *OOH, are bound to the active site by oxygen with a single bond in consistent with the above-mentioned $4e^-$ mechanism. The Gibbs free energy difference value of $Fe_{0.25}Co_{0.75}P$ ($\Delta G_{II} = 0.56$ eV) is lower than that of CoP ($\Delta G_{II} = 1.29$ eV) and FeP ($\Delta G_{II} = 0.56$ eV), suggesting that $Fe_{0.25}Co_{0.75}P$ needs a smaller overpotential to drive water oxidation. Furthermore, the results are well consistent with the much lower calculated overpotential (0.06 V) for $Fe_{0.25}Co_{0.75}P$ than that of CoP (1.0 V) and FeP (0.59 V) (Fig. 6e and f and Fig. S37b). This step is considered as the rate determining step for OER process, which is the same for these two electrocatalysts. These results suggest that the electronic structure of $Fe_{0.25}Co_{0.75}P$ is modulated by Fe doping, which can optimize the adsorption energies of the OER intermediates to the optimal values. In order to further verify whether Ni foam could react during the process of phosphorization, sulfuration or selenization and influence the surface composition of Ni foam, the electrochemical performance of the pure Ni foams treated by phosphorization (Ni foam-P), sulfuration (Ni foam-S), selenization (Ni foam-Se) were tested respectively. We can observe that the HER activity and OER activity of obtained samples are very low (Fig. S38). This further confirms that $Fe_{0.29}Co_{0.71}P$ itself is the active material for HER and OER.

The overall water splitting performance of $Fe_{0.29}Co_{0.71}P$/NF was evaluated in a two-electrode system using $Fe_{0.29}Co_{0.71}P$/NF as both the cathode and anode. The $Fe_{0.29}Co_{0.71}P$/NF couple exhibited superior electrocatalytic activity and long-time stability. To reach 10 mA cm^{-2}, it only needed 1.59 V of cell voltage, which is better than the IrO_2//Pt/C (1.61 V) and FeP//CoP (1.70 V) couple (Fig. S39a). To produce a larger current density of 50 and 100 mA cm^{-2}, it only needed 1.67 and 1.69 V of cell voltages, respectively (Video S1), which is evidently better than or close to many other recently reported high-performance overall water electrocatalysts (Table S5) [46]. Meanwhile, the long-term durability of $Fe_{0.29}Co_{0.71}P$ electrolyzer was tested at diverse current densities through the successive current step from 10 to 180 mA cm^{-2} (Fig. S39b), where relatively smooth curves at all current densities could be observed, demonstrating the good stability even at a high current density of 180 mA cm^{-2}. After continuous current step test of 110 h, the current density was restored to 10 mA cm^{-2}. The cell voltages of $Fe_{0.29}Co_{0.71}P$ electrolyzer remained stable and slightly decreased than those during continuous current step test at 10 mA cm^{-2}. These results confirmed that the $Fe_{0.29}Co_{0.71}P$ electrolyzer has superior stability for the water splitting, especially at a high current density.

Theoretical calculation section is available in the Supporting Information.

Supplementary video related to this article can be found at https://doi.org/10.1016/j.nanoen.2019.104174.

4. Conclusions

In summary, Fe doping was demonstrated to significantly improve the HER and OER activity of $Fe_{0.29}Co_{0.71}P$ by rationally modifying the electron densities of catalytic sites. XPS and DFT calculation consistently elucidate that Fe doping can effectively optimize the electronic structure of $Fe_{0.29}Co_{0.71}P$. It makes Co positively charged and P negatively charged which can promote water molecule adsorption and activation and weaken the bond energy of P-H_{ads}. The modified electronic structure can well optimize the adsorption and desorption of H on the surface of electrocatalysts, and can efficiently accelerate Volmer and Heyrovsky steps of HER and achieve high HER activity in alkaline media. In addition, as expected, the prepared low-cost $Fe_{0.29}Co_{0.71}P$ catalyst exhibits evidently improved electrocatalytic activity and durability for water splitting. More importantly, this work not only provides a facile and universal method to optimize adsorption and desorption of H atoms, but also develops a kind of high performance metal phosphide-based electrocatalysts for water splitting in alkaline media.

Acknowledgements

The study was financially supported by Projects 51579096, 51521006 and 51222805 supported by National Natural Science Foundation of China, the Key Research and Development Project of Hunan Province of China (2017SK2241), the National Innovative Talent Promotion Program of China (2017RA2088), the Funds for Innovative Province Construction of Hunan Province of China (2019RS3012), the National Program for Support of Top–Notch Young Professionals of China (2012).

Appendix A. Supplementary data

Supplementary data to this article can be found online at https://doi.org/10.1016/j.nanoen.2019.104174.

References

[1] W.S. Zhi, J. Kibsgaard, C.F. Dickens, I. Chorkendorff, J.K. Nørskov, T.F. Jaramillo, Science, Combining theory and experiment in electrocatalysis: insights into materials design, Science 355 (2017) 4998.
[2] M.S. Dresselhaus, I.L. Thomas, Alternative energy technologies, Nature 414 (2001) 332.
[3] P. Wang, K. Jiang, G. Wang, J. Yao, X. Huang, Phase and interface engineering of platinum–nickel nanowires for efficient electrochemical hydrogen evolution, Angew. Chem. Int. Ed. 55 (2016) 12859–12863.
[4] M.A. Lukowski, A.S. Daniel, F. Meng, A. Forticaux, L. Li, S. Jin, Enhanced hydrogen evolution catalysis from chemically exfoliated metallic MoS_2 nanosheets, J. Am. Chem. Soc. 135 (2013) 10274–10277.
[5] D. Kong, H. Wang, Z. Lu, Y. Cui, $CoSe_2$ nanoparticles grown on carbon fiber paper: an efficient and stable electrocatalyst for hydrogen evolution reaction, J. Am. Chem. Soc. 136 (2014) 4897–4900.
[6] S. Wang, J. Wang, M. Zhu, X. Bao, B. Xiao, D. Su, H. Li, Y. Wang, Molybdenum carbide-modified nitrogen-doped carbon vesicle encap-sulating nickel nanoparticles: a highly efficient, low-cost catalyst for hydrogen evolution reaction, J. Am. Chem. Soc. 137 (2015), 15753-15759.
[7] Y. Shi, B. Zhang, Recent advances in transition metal phosphide nanomaterials: synthesis and applications in hydrogen evolution reaction, Chem. Soc. Rev. 45 (2016) 1781.
[8] C. Tang, L. Gan, R. Zhang, W. Lu, X. Jiang, A.M. Asiri, X. Sun, J. Wang, L. Chen, Ternary $Fe_xCo_{1-x}P$ nanowire array as a robust hydrogen evolution reaction electrocatalyst with Pt-like activity: experimental and theoretical insight, Nano Lett. 16 (2016) 6617.
[9] E.J. Popczun, J.R. Mckone, C.G. Read, A.J. Biacchi, A.M. Wiltrout, N.S. Lewis, R. E. Schaak, Nanostructured nickel phosphide as an electrocatalyst for the hydrogen evolution reaction, J. Am. Chem. Soc. 135 (2013) 9267–9270.
[10] P. Xiao, M.A. Sk, L. Thia, X. Ge, R.J. Lim, J.Y. Wang, K.H. Lim, X. Wang, Molybdenum phosphide as an efficient electrocatalyst for the hydrogen evolution reaction, Energy Environ. Sci. 7 (2014) 2624–2629.
[11] H. Yang, Y. Zhang, F. Hu, Q. Wang, Urchin-like CoP nanocrystals as hydrogen evolution reaction and oxygen reduction reaction dual-electrocatalyst with superior stability, Nano Lett. 15 (2015) 7616.
[12] Q. Liu, J. Tian, W. Cui, P. Jiang, N. Cheng, A.M. Asiri, X. Sun, Carbon nanotubes decorated with CoP nanocrystals: a highly active non-noble-metal nanohybrid electrocatalyst for hydrogen evolution, Angew. Chem. Int. Ed. 126 (2014) 6828–6832.
[13] Y. Deng, L. Tang, C. Feng, G. Zeng, J. Wang, Y. Zhou, Y. Liu, B. Peng, H. Feng, Construction of plasmonic Ag modified phosphorous-doped ultrathin g-C_3N_4 nanosheets/$BiVO_4$ photocatalyst with enhanced visible-near-infrared response ability for ciprofloxacin degradation, J. Hazard Mater. 344 (2017) 758–769.
[14] J. Wang, L. Tang, G. Zeng, Y. Deng, Y. Liu, L. Wang, Y. Zhou, G. Zhi, J. Wang, Z. Chen, Atomic scale g-C_3N_4/Bi_2 $WO_6$2D/2D heterojunction with enhanced photocatalytic degradation of ibuprofen under visible light irradiation, Appl. Catal. B Environ. 209 (2017) 285–294.
[15] L. Tang, H. Feng, J. Tang, G. Zeng, Y. Deng, J. Wang, Y. Liu, Y. Zhou, Treatment of arsenic in acid wastewater and river sediment by Fe@Fe_2O_3 nanobunches: the effect of environmental conditions and reaction mechanism, Water Res 117 (2017) 175.
[16] Y. Deng, L. Tang, G. Zeng, Z. Zhu, Y. Ming, Y. Zhou, J. Wang, Y. Liu, J. Wang, Insight into highly efficient simultaneous photocatalytic removal of Cr(VI) and 2,4-diclorophenol under visible light irradiation by phosphorus doped porous ultrathin g-C_3N_4 nanosheets from aqueous media: performance and reaction mechanism, Appl. Catal. B Environ. 203 (2017) 343–354.
[17] L. Tang, G. Yang, G. Zeng, Y. Cai, S. Li, Y. Zhou, Synergistic effect of iron doped ordered mesoporous carbon on adsorption-coupled reduction of hexavalent chromium and the relative mechanism study, Chem. Eng. J. 239 (2014) 114–122.
[18] Z.H. Xue, S. Hui, Q.Y. Yu, Z. Bing, H.H. Wang, X.H. Li, J.S. Chen, Janus Co/CoP nanoparticles as efficient Mott–Schottky electrocatalysts for overall water splitting in wide pH range, Adv. Energ. Mater. 7 (2017) 1602355.
[19] Z. Lei, J. Shan, Y. Liu, M. Shao, D. Xue, Ultrathin CoNiP@layered double hydroxides core-shell nanosheets arrays for largely enhanced overall water splitting, ACS Appl. Energy Mater. 1 (2018), 00151.
[20] B. Zhang, Y.H. Lui, G. Aps, B. Chen, X. Tang, Z. Qi, S. Hu, Hierarchical FeNiP @ ultrathin carbon nanoflakes as alkaline oxygen evolution and acidic hydrogen evolution catalyst for efficient water electrolysis and organic decomposition, ACS Appl. Mater. Interfaces 10 (2018) 8739–8748.
[21] G. Kresse, J. Furthmüller, Efficiency of ab-initio total energy calculations for metals and semiconductors using a plane-wave basis set, Comp. Mat. Er. Sci. 6 (1996) 15–50.
[22] G. Kresse, J. Hafner, Ab initio molecular-dynamics simulation of the liquid-metal–amorphous-semiconductor transition in germanium, Phys. Rev. B 47 (1993) 558.
[23] G. Kresse, D. Joubert, From ultrasoft pseudopotentials to the projector augmented-wave method, Phys. Rev. B 59 (1999) 1758–1775.
[24] P.E. Blöchl, Projector augmented-wave method, Phys. Rev. B 50 (1994) 17953–17979.
[25] J.P. Perdew, K. Burke, M. Ernzerhof, ERRATA:Generalized gradient approximation made simple, Phys. Rev. Lett. 77 (1998) 3865–3868.
[26] H. Ali, C. Huanlin, S. Zijun, X. Jun, D. Pingwu, High catalytic activity for water oxidation based on nanostructured nickel phosphide precursors, Chem. Commun. 51 (2015) 11626–11629.
[27] L.-A. Stern, L. Feng, S. Fang, X. Hu, Ni_2P as a Janus catalyst for water splitting: the oxygen evolution activity of Ni_2P nanoparticles, Energy Environ. Sci. 8 (2015) 2347–2351.
[28] H. Liang, A.N. Gandi, D.H. Anjum, X. Wang, U. Schwingenschlögl, H.N. Alshareef, Plasma-assisted synthesis of NiCoP for efficient overall water splitting, Nano Lett. 16 (2016) 7718–7725.
[29] J. Tian, Q. Liu, A.M. Asiri, X. Sun, Self-supported nanoporous cobalt phosphide nanowire arrays: an efficient 3D hydrogen-evolving cathode over the wide range of pH 0-14, J. Am. Chem. Soc. 136 (2014) 7587–7590.
[30] B.W. Zhang, T. Sheng, Y.D. Liu, Y.X. Wang, L. Zhang, W.H. Lai, L. Wang, J. Yang, Q.F. Gu, S.L. Chou, H.K. Liu, S.X. Dou, Atomic cobalt as an efficient electrocatalyst in sulfur cathodes for superior room-temperature sodium-sulfur batteries, Nat. Commun. 9 (2018) 4082.
[31] P. Jiang, Q. Liu, Y. Liang, J. Tian, A.M. Asiri, X. Sun, A cost-effective 3D hydrogen evolution cathode with high catalytic activity: FeP nanowire array as the active phase, Angew. Chem. Int. Ed. 126 (2015) 13069–13073.
[32] X. Long, G. Li, Z. Wang, H. Zhu, T. Zhang, S. Xiao, W. Guo, S. Yang, Metallic iron-nickel sulfide ultrathin nanosheets as a highly active electrocatalyst for hydrogen evolution reaction in acidic media, J. Am. Chem. Soc. 137 (2015) 11900–11903.
[33] E. Popczun, C. Roske, C. Read, J.C. Crompton, J. Mcenaney, J. Callejas, N. Lewis, R. Schaak, Highly branched cobalt phosphide nanostructures for hydrogen-evolution electrocatalysis, J. Mater. Chem. A 3 (2015) 5420–5425.
[34] L. Jiao, Y.X. Zhou, H.L. Jiang, Metal-organic framework-based CoP/reduced graphene oxide: high-performance bifunctional electrocatalyst for overall water splitting, Chem. Sci. 7 (2016) 1690–1695.
[35] J.F. Callejas, C.G. Read, E.J. Popczun, J.M. Mcenaney, R.E. Schaak, Nanostructured Co_2P electrocatalyst for the hydrogen evolution reaction and direct comparison with morphologically equivalent CoP, Chem. Mater. 27 (2015) 3769–3774.
[36] J. Huang, S. Ying, Y. Zhang, W. Wu, C. Wu, Y. Sun, R. Lu, G. Zou, Y. Li, X. Jie, FeO_x/FeP hybrid nanorods neutral hydrogen evolution electrocatalysis: insight into interface, J. Mater. Chem. A 6 (2018) 9467–9472.
[37] J.F. Callejas, J.M. Mcenaney, C.G. Read, J.C. Crompton, A.J. Biacchi, E.J. Popczun, T.R. Gordon, N.S. Lewis, R.E. Schaak, Electrocatalytic and photocatalytic hydrogen production from acidic and neutral-pH aqueous solutions using iron phosphide nanoparticles, ACS Nano 8 (2014) 11101–11107.
[38] J. Tian, Q. Liu, Y. Liang, Z. Xing, A.M. Asiri, X. Sun, FeP nanoparticles film grown on carbon cloth: an ultrahighly active 3D hydrogen evolution cathode in both acidic and neutral solutions, ACS Appl. Mater. Interfaces 6 (2014) 20579–20584.
[39] M.J. Kale, T. Avanesian, P. Christopher, Direct photocatalysis by plasmonic nanostructures, ACS Catal. 4 (2014) 116–128.

[40] P. Liu, J. Zhu, J. Zhang, P. Xi, K. Tao, D. Gao, D. Xue, P dopants triggered new basal plane active sites and enlarged interlayer spacing in MoS_2 nanosheets toward electrocatalytic hydrogen evolution, ACS Energ. Lett. 2 (2017) 745–752.
[41] B. Hammer, J.K. Nørskov, Erratum to Electronic factors determining the reactivity of metal surfaces, Surf. Sci. 359 (1996) 306.
[42] A. Vojvodic, J.K. Nørskov, F. Abild-Pedersen, Electronic structure effects in transition metal surface chemistry, Top. Catal. 57 (2014) 25–32.
[43] H. Xin, A. Vojvodic, J. Voss, J.K. Nørskov, F. Abild-Pedersen, Effects of d-band shape on the surface reactivity of transition-metal alloys, Phys. Rev. B 89 (2014) 867–875.
[44] N. Acerbi, S.C.E. Tsang, G. Jones, S. Golunski, P. Collier, Rationalization of interactions in precious metal/ceria catalysts using the d-band center model, Angew. Chem. Int. Ed. 125 (2013) 7891–7895.
[45] P. Li, X. Duan, K. Yun, Y. Li, G. Zhang, L. Wen, X. Sun, Tuning electronic structure of NiFe layered double hydroxides with vanadium doping toward high efficient electrocatalytic water oxidation, Adv. Energ. Mater. (2018) 1703341.
[46] X. Wang, W. Li, D. Xiong, D.Y. Petrovykh, L. Liu, Bifunctional nickel phosphide nanocatalysts supported on carbon fiber paper for highly efficient and stable overall water splitting, Adv. Funct. Mater. 26 (2016) 4067–4077.

Haopeng Feng is currently a Ph.D. candidate under the supervision of Prof. Lin Tang at College of Environmental Science and Engineering in Hunan University, China. He received his Bachelor's degree (2015) in Shandong University of Technology in China. His current research focuses on synthesis and application of iron-based nanomaterials in electrocatalytical water splitting.

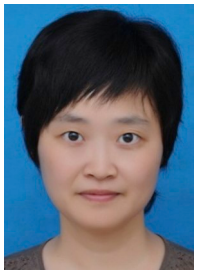

Prof. Lin Tang is currently a professor at College of Environmental Science and Engineering in Hunan University, China. She received a Ph.D. degree (2009) from Hunan University in the field of nanomaterials and nanosensors for environmental pollution control. She worked as a visiting scientist in Columbia University, USA from 2012 to 2013. Her research interests focus on the synthesis and application of nanomaterials for advanced oxidation process.

Prof. Guangming Zeng is currently a professor and the head of College of Environmental Science and Engineering in Hunan University, China. He received a Ph.D. degree from Wuhan University and began to work in Hunan University in 1988. He is one of the Highly Cited Researchers in the world issued by Clarivate Analytics (2017 and 2018). His current research interests focus on the synthesis and application of functional nanomaterials in the environment and energy field.

Jiangfang Yu is currently a Ph.D. candidate under the supervision of Prof. Lin Tang at College of Environmental Science and Engineering in Hunan University, China. She received her Bachelor's degree (2016) in Hunan University in China. Her current research focuses on the electron transfer pathways in advanced oxidation process.

Dr. Yaocheng Deng is currently an associate professor at College of Resources and Environment in Hunan Agricultural University, China. He received a Ph.D. degree (2018) from Hunan University in the field of nanomaterials and photocatalysis. His research interests focus on the photocatalysis and electrocatalysis for energy and environment applications.

Prof. Yaoyu Zhou is currently a professor at College of Resources and Environment in Hunan Agricultural University, China. He received a Ph.D. degree (2016) from Hunan University in the field of nanomaterials and nanosensors for environmental pollution control. He has been working as a postdoctor at The Hong Kong Polytechnic University since 2018. His research interests focus on the synthesis and application of nanoporous materials.

Jingjing Wang is currently a Ph.D. candidate under the supervision of Prof. Lin Tang at College of Environmental Science and Engineering in Hunan University, China. She received her Master's degree (2016) in Hunan University, China. Her current research interests mainly focus on synthesis of functional nanohybrid and nanoporous materials.

Chengyang Feng is currently a Ph.D. candidate under the supervision of Prof. Lin Tang at College of Environmental Science and Engineering in Hunan University, China. He received his Bachelor's degree (2016) in Harbin Engineering University in China. His current research focuses on the synthesis of nanomaterials for photocatalysis and DFT study.

Ting Luo is currently a Master candidate under the supervision of Prof. Lin Tang at College of Environmental Science and Engineering in Hunan University, China. She received her Bachelor's degree (2018) in Hunan University, China. Her current research focuses on the synthesis and application of iron-based nanomaterials in electrocatalysis.

Binbin Shao is currently a Ph.D. candidate at College of Environmental Science and Engineering in Hunan University, China. He received his Bachelor's degree (2015) in Jiangxi University of Science and Technology in China. His current research focuses on the synthesis of nanocatalysts for environment and energy applications.